A General Approach to Sampled-Data Modeling for Ripple-Based Control—Part I: Peak/Valley Current Mode and Peak/Valley Voltage Mode

Na Yan, Xinbo Ruan, *Fellow, IEEE*, and Xin Li, *Member, IEEE*

***Abstract*—This article is aiming to unify the modeling methods for various ripple-based control schemes. It is divided into two parts, and the first part presents a sampled-data modeling method for the peak/valley current mode (PCM/VCM) control and the peak/valley voltage mode (PVM/VVM) control. It is pointed out that due to the high bandwidth of the dc–dc converter under PCM/VCM or PVM/VVM control, the sideband effect cannot be ignored in the modeling process. Meanwhile, with the small-signal assumption, the feedback perturbation signal has a discontinuity of the first kind at each sampling instant, so the perturbation value at this instant should be obtained according to the Dirichlet conditions, which is equal to half of the sum of the limit values on the left and right sides of the signal. Then, by using Shannon's sampling theorem, the transfer functions of the modulator and the loop gain are derived, and they are used to analyze the influence of the sideband components on the converter stability. Finally, the experimental results from a PCM controlled buck converter validate the proposed modeling technique.**

***Index Terms*—A discontinuity of the first kind, modulator, ripple-based control, sampled-data modeling, sideband effect.**

I. Introduction

MODERN microprocessors have been finding wide applications. The buck converter is usually adopted for powering the microprocessors due to its simplicity, and it is required to have fast transient response. Various ripple-based control schemes for meeting this requirement have attracted a lot of attention [1]–[4]. In the ripple-based control, the switching ripple of the current or voltage is used as the ramp of the modulator to compare with the reference to generate the drive signals for the switches [5]–[7]. Compared with the average voltage/current mode (AVM/ACM) control [8]–[11], ripple-based control has a simpler structure and better dynamic performance. In this article, the control schemes that utilize the current feedback signal as the input of the modulator are named as current-mode ripple-based control, including peak/valley current mode (PCM/VCM) control [11]–[13] and current-mode constant ON/OFF time control (C-COT/C-COFT) [14], [15], and the control schemes that adopt the voltage feedback signal as the input of the modulator are named as voltage-mode ripple-based control, including peak/valley voltage mode (PVM/VVM) control [5], [14], and voltage-mode constant ON/OFF time control [14], [16].

For the ripple-based control, the control parameters and the circuit parameters such as equivalent series resistor (ESR) of the output capacitor should be carefully designed to avoid instability, especially fast-scale instability [5], [6], [16]. For example, subharmonic instability occurs when the duty cycle exceeds 0.5 in a PCM controlled dc–dc converter, and a smaller time constant of the output capacitor will lead to instability in a buck converter with voltage-mode ripple-based control. There are also some interesting phenomena. For example, a C-COT/ C-COFT controlled buck converter is always stable at any duty cycle. In order to explain the abovementioned stability cases and optimize the circuit parameters design, the modeling of the ripple-based control is an essential topic.

The key challenge of modeling a dc–dc converter with ripple-based control is the modeling of the modulator. Various modeling methods have been proposed for ripple-based control [15], [34], however, only a few articles gave the small-signal model of the modulator and the obtained results are not verified. Furthermore, the obtained models are different and a consensus has not been reached. Hence, a unified modeling method of the modulator that is accurate, simple, and suitable for all kinds of ripple-based control is expected, which is the main purpose of this article. This article is divided into two parts. Part I discusses the PCM/VCM and PVM/VVM control, and Part II focuses on the COT and COFT control.

Among the existing modeling techniques for a PCM/VCM controlled dc–dc converter, the biggest controversy is the derivation of the modulator gain factor F_m, which is the minus of the ratio of the duty cycle perturbation and the current feedback perturbation. Fig. 1 shows the key waveforms of the PCM control, where, i_s is the feedback current and $\hat{i}_s$ is its perturbation; m_1 and $-m_2$ are the slopes of i_s during the ON-time and OFF-time of the switch, respectively, m_c is the slope of the compensation ramp, and T_s is the switching period. Table I lists the values of F_m obtained in [11] and [23]–[28], and the differences are caused by different values of $\hat{i}_s$ selected at the sampling instant, i.e., the

Manuscript received February 18, 2021; revised July 7, 2021 and October 2, 2021; accepted November 20, 2021. Date of publication December 6, 2021; date of current version February 18, 2022. This work was supported by the National Science Foundation of China for Distinguished Young Scholars under Grant 51525701. Recommended for publication by Associate Editor L. Corradini. *(Corresponding author: Xinbo Ruan.)*

Na Yan and Xinbo Ruan are with the Center for More-Electric-Aircraft Power System, College of Automation Engineering, Nanjing University of Aeronautics and Astronautics, Nanjing 211106, China (e-mail: yanna@nuaa.edu.cn; ruanxb@nuaa.edu.cn).

Xin Li is with the School of Electrical and Electronic Engineering, Nanyang Technological University, 639798, Singapore (e-mail: li-xin@ntu.edu.sg).

Color versions of one or more figures in this article are available at https://doi.org/10.1109/TPEL.2021.3132619.

Digital Object Identifier 10.1109/TPEL.2021.3132619

TABLE I
VALUE OF F_{m} FOR PCM IN THE EXISTING LITERATURE

Sources of F_{m}	The derivation of F_{m}
from (50b) in [23] or from (2) in [24]	$\hat{i}_{\mathrm{s1}}(k)=-(m_1+m_{\mathrm{c}})\hat{d}(k)T_{\mathrm{s}} \Rightarrow F_{\mathrm{m}}=-\dfrac{\hat{d}(k)}{\hat{i}_{\mathrm{s1}}(k)}=\dfrac{1}{(m_1+m_{\mathrm{c}})T_{\mathrm{s}}}$
from (38) and (39) in [25]	$i_1=I_{\mathrm{ref}}-m_{\mathrm{c}}d(k)T_{\mathrm{s}}-\dfrac{m_1}{2}d(k)T_{\mathrm{s}} \Rightarrow F_{\mathrm{m}}=-\dfrac{\hat{d}(k)}{\hat{i}_1}=\dfrac{1}{(m_1/2+m_{\mathrm{c}})T_{\mathrm{s}}}$
from (31) in [26]	$i_2=I_{\mathrm{ref}}-m_{\mathrm{c}}d(k)T_{\mathrm{s}}-\dfrac{m_2}{2}\left(T_{\mathrm{s}}-d(k)T_{\mathrm{s}}\right) \Rightarrow F_{\mathrm{m}}=-\dfrac{\hat{d}(k)}{\hat{i}_2}=\dfrac{1}{(-m_2/2+m_{\mathrm{c}})T_{\mathrm{s}}}$
from (12.66) in [11] or from (1) and (4) in [27]	$\langle i\rangle_{T_{\mathrm{s}}}=di_1+(1-d)i_2=I_{\mathrm{ref}}-m_{\mathrm{c}}d(k)T_{\mathrm{s}}-\dfrac{m_1}{2}d(k)^2T_{\mathrm{s}}-\dfrac{m_2}{2}\left(1-d(k)\right)^2T_{\mathrm{s}} \Rightarrow F_{\mathrm{m}}=-\dfrac{\hat{d}(k)}{\langle\hat{i}\rangle_{T_{\mathrm{s}}}}=\dfrac{1}{m_{\mathrm{c}}T_{\mathrm{s}}}$
from (15), (16) and (17) in [28]	$\left.\begin{aligned}\hat{i}_{\mathrm{s2}}(k)&=-(m_1+m_{\mathrm{c}})\hat{d}(k+1)T_{\mathrm{s}}\\ \hat{i}_{\mathrm{s2}}(k+1)&=(m_2-m_{\mathrm{c}})\hat{d}(k+1)T_{\mathrm{s}}\end{aligned}\right\} \Rightarrow F_{\mathrm{m}}=-\dfrac{\hat{d}(k+1)}{\hat{i}_{\mathrm{s2}}(k+1)}\Big\vert_{\hat{i}_{\mathrm{s2}}(k+1)\approx\hat{i}_{\mathrm{s2}}(k)} \approx \dfrac{2}{(m_1-m_2+2m_{\mathrm{c}})T_{\mathrm{s}}}$

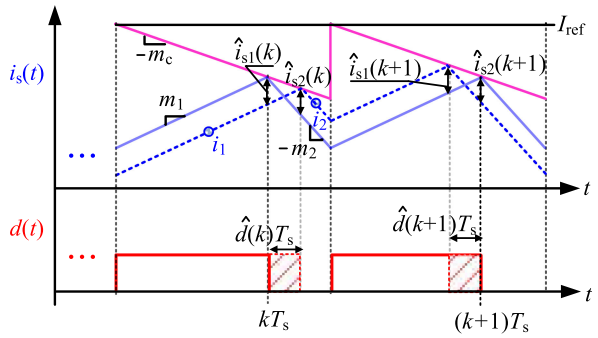

Fig. 1. Key waveforms of the modulator for PCM in steady state.

intersection instant of two input signals of the modulator. In [23] and [24], the value of $\hat{i}_s$ right before the sampling instant, i.e., the value of $\hat{i}_{s1}(k)$ in Fig. 1, is used. In [25], the average value of $\hat{i}_s$ during the switch-ON time, which is derived from the value of i_1, is used, while in [26] the average value of $\hat{i}_s$ during the switch-OFF time (derived from i_2) is discussed. In [11] and [27], the average value of $\hat{i}_s$ during a switching period, expressed as $\langle i\rangle_{T\mathrm{s}}$, is used. In [28], the F_m is obtained with the assumption of $\hat{i}_{s2}(k)=\hat{i}_{s2}(k+1)$. In addition to the controversy for the derivation of F_m, the expressions of the loop gain obtained in different articles are also different.

In most existing modeling methods for the PVM/VVM controlled buck converter, it is assumed that the ESR of the output capacitor is so larger that the switching component in the output voltage is the voltage across ESR resulted by the inductor current ripple. In this case, the PVM/VVM control is equivalent to the PCM/VCM control, and the ESR is the inductor current sense gain, and the existing modeling methods for PCM/VCM can be directly applied to the PVM/VVM control [30]–[33]. Hence, these methods not only face the similar inaccuracy issue as those for PCM/VCM, but also not that general due to the assumption of the larger ESR.

In [5], [17], and [29], the closed-loop gains are derived, respectively, by using the Krylov–Bogoliubov–Mitropolsky method and the describing function method for ripple-based control. However, these two methods require cumbersome mathematical derivation and provide quite limited physical insights, which restrict their practical usefulness.

It should be noted that in all the above modeling methods for ripple-based control, the closed-loop gains are derived first since it is difficult to establish the transfer function of the modulator directly in the past. In these methods, it is all mentioned that the nonlinear characteristic of the modulator, i.e., the sampling characteristic of the modulator, plays an important role in the converter stability. However, no method reveals exactly how this characteristic affects the dynamic performance, and the modeling techniques for the modulator are also unclear.

Fortunately, some modeling methods that considered the influence of sideband components, which is caused by the sampling characteristic of the modulator, can provide some inspiration to modeling the modulator under the PCM/VCM/PVM/VVM control and are reviewed as follows.

In [35], the power stage and the modulator are regarded as a whole part, and its transfer function is derived by approximating the perturbation in the duty cycle signal, which contains a series of narrow pulse signals, to a train of impulse signals. Also, the obtained results indicate that the loop gain measured with the feedback loop open is not the same as that measured with the feedback loop closed (see (11.5) and (11.16a) in [35]), which is caused by the sideband effect. In [36], the effect of the sideband component at s–$j\omega_s$ (ω_s is the switching angular frequency) is taken into consideration for the loop gain of the buck converter with the AVM control, and the path which describes this effect is introduced into the control block diagram, thus providing a clear physical insight about the sideband effect. The effect of other sideband components on the loop gain is further considered in [37] and [38]. Compared with [35], it is revealed in [36]–[38] that the difference of the loop gains with the feedback loop open and closed is confirmedly caused by the sideband effect on the frequency response of the modulator, thus indicating the importance of directly modeling the modulator based on the accurate frequency analysis.

From these methods of studying the sideband effect, it can be found that when two signals intersect at a fixed time in

each switching period to generate the duty cycle signal, such a process can be regarded as a sampler, and the intersection moment is the sampling instant. That is to say, the modulators in the ripple-based control and the AVM/ACM control are a sampler from the perspective of small-signal analysis. So, the sampling principle can be used to directly derive the transfer function of the modulator, which implies the consistency of modeling methods of the modulator in the AVM/ACM and PCM/VCM/PVM/VVM control. However, the existing modeling methods for ripple-based control are quite different from those for AVM [36]–[38], keeping us from a unified understanding of all the basic control schemes.

In this part, a method to derive the transfer function of the modulator, including the exact definition of F_m, for PCM/VCM is proposed by directly using the sampling theorem, and then it is further extended to the PVM/VVM control. Since the derivation process is based on the sampling characteristics of the modulator, the proposed modeling method is referred to as the *sampled-data modeling method*.

The rest of this article is organized as follows. Section II introduces the sampling characteristic of the modulator, and then presents the sampled-data modeling method for the PCM/VCM controlled buck converter followed by the stability analysis and the comparison with other existing well-known models. Section III derives the small-signal models of the buck converter with the PVM/VVM control, analyzes the influence of the sideband effect on the converter stability, and determines the stability conditions which the time constant of the output capacitor need to satisfy. Then, the obtained results are verified by simulation. Section IV discusses the extension of the proposed sampled-data modeling method to other dc–dc converters. The experimental results of a PCM controlled buck converter are provided in Section V. Finally, Section VI concludes this article.

II. Sampled-Data Modeling for PCM/VCM

In this section, the sampled-data modeling for the dc–dc converter under the PCM/VCM control is developed first based on the sampling characteristic of the modulator. Then, the obtained theoretical models are used to analyze the converter stability and further verified by simulation.

A. Sampling Characteristic of the Modulator

Fig. 2 shows a PCM/VCM controlled buck converter, where $V_{\rm in}$ is the input voltage, L_f is the filter inductor, C_f is the output capacitor, R_c is the ESR of C_f, $R_{\rm Ld}$ is the load resistor, i_L is the inductor current, i_s is its feedback signal, d is the duty cycle signal, $H_{\rm i}$ is the inductor current sense gain, and m_c is the slope of the compensation ramp, T_s is the switching period, and the corresponding switching (angular) frequency is represented by $f_s(\omega_s)$. The part from the feedback signal to the duty cycle signal is referred to as the modulator. PCM is taken as an example to present the sampling characteristic of the modulator and derive its small-signal model here.

If the modulator in Fig. 2 is a sampler, it means that when an ac small signal $v_{\rm ac}$ with the (angular) frequency of f_p (ω_p) is injected into the point A shown in Fig. 2 (note that $v_{\rm ac}$ contains the ac components at the frequencies $\pm\omega_p$ in the complex frequency domain), the perturbation components in the feedback current and the duty cycle, denoted as $\hat{i}_s$ and $\hat{d}$, respectively, will both contain the ac components at the frequencies $\pm\omega_p+n\omega_s(n\in\mathbb{Z})$, denoted as $\hat{i}_s(\pm j\omega_p+jn\omega_s)$ and $\hat{d}(\pm j\omega_p+jn\omega_s)$, respectively. The $\pm\omega_p+n\omega_s$ components ($n\neq 0$) are called the sideband components. It should be mentioned that the components in $\hat{d}$ at the frequencies $\omega_p+n\omega_s$ ($n\in\mathbb{Z}$) are generated by $\hat{i}_s(j\omega_p+jn\omega_s)$, while $\hat{d}(-j\omega_p+jn\omega_s)$ are generated by $\hat{i}_s(-j\omega_p+jn\omega_s)$, which means it does not need to consider $\hat{i}_s(-j\omega_p+jn\omega_s)$ and $\hat{d}(-j\omega_p+jn\omega_s)$ when deriving the relationship between $\hat{d}(j\omega_p+jn\omega_s)$ and $\hat{i}_s(j\omega_p+jn\omega_s)$.

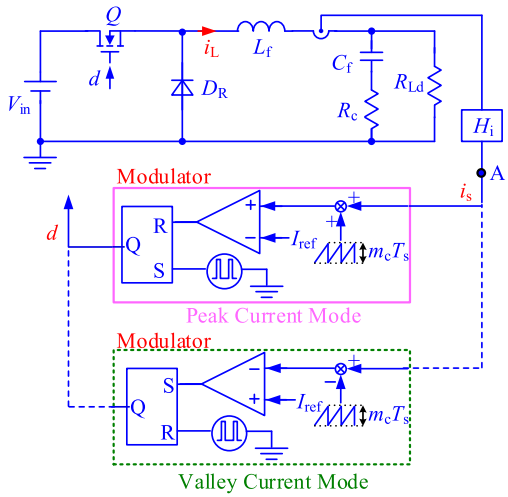

Fig. 2. PCM/VCM controlled buck converter.

TABLE II
Simulated Buck Converter Parameters

Parameters	Symbols	Values	Parameters	Symbols	Values
Input votlage	$V_{\rm in}$ / V	12	Inductance	$L_{\rm f}$ / μH	6
Output voltage	$V_{\rm o}$ / V	3.3	ESR of the inductor	$R_{\rm L}$ / mΩ	20
Output power	$P_{\rm o}$ / W	33	Output capacitance	$C_{\rm f}$ / μF	200
Load	$R_{\rm Ld}$ / Ω	1/3	ESR of the capacitor	$R_{\rm c}$ / mΩ	10
Switching frequency	$f_{\rm s}$ / Hz	100k	Current sensed gain	$H_{\rm i}$	0.1

In order to verify the sampling characteristic of the modulator, the PCM controlled buck converter in Table II is built in Simplis software. The steady-state operating point is first obtained, and then an ac signal with a frequency of 2 kHz and an amplitude of 1 mV is injected into the feedback current i_s for further simulation. The time-domain waveforms are obtained by subtracting the steady-state waveforms from those with perturbations, as shown in Fig. 3. After that, Fourier analysis tool in Simplis is adopted to extract the frequency spectra of time-domain waveforms.

As seen from Fig. 3, both $\hat{i}_s$ and $\hat{d}$ contain not only the ac component at 2 kHz, but also the components at sideband frequencies, and the sideband components in $\hat{i}_s$ are obviously not ignorable compared to that of the perturbation frequency. The amplitudes of the components in $\hat{d}$ at all sideband frequencies

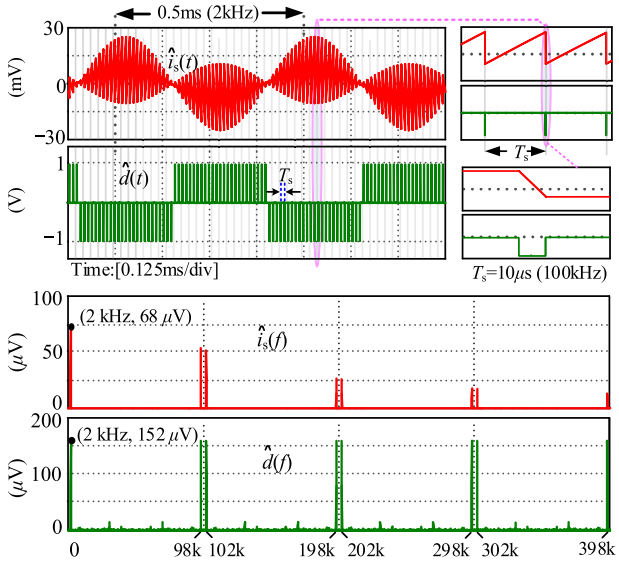

Fig. 3. Simulated waveforms of $\hat{i}_s$ and $\hat{d}$ when a 1 mV, 2 kHz perturbation is injected into i_s.

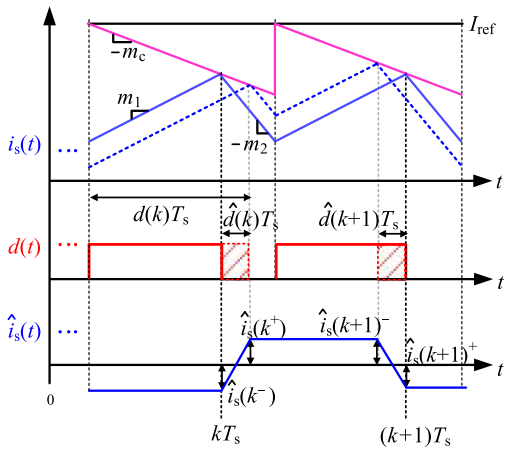

Fig. 4. Key waveforms of the modulator in the perturbed state under PCM.

and the perturbation frequency are all equal, thus verifying the sampling characteristic of the modulator. The next section will directly use the sampling theorem to derive the transfer function of the modulator.

B. Sampled-Data Modeling

Fig. 4 shows the operating principle of the modulator. The intersection instant of two input signals of the modulator, i.e., the sampling instant, is selected as the beginning time in each cycle to simplify the derivation process. As seen from Fig. 4, i_s and d are negative correlated, i.e., the greater i_s, the lower the d. Hence, the transfer function of the modulator $G_{\rm PWM}(s)$ is defined as

$$G_{\rm PWM}(s) \triangleq -\frac{\hat{d}(s)}{\hat{i}_s(s)}. \tag{1}$$

Denoting $\hat{d}(k)$ and $\hat{i}_s(k)$ as the value of $\hat{d}$ and $\hat{i}_s$ at the kth sampling instant, F_m is defined as

$$F_m \triangleq -\frac{\hat{d}(k)}{\hat{i}_s(k)}. \tag{2}$$

As seen from Figs. 3 and 4, $\hat{i}_s$ has a discontinuity of the first kind at each sampling instant under the assumption of the small perturbation signal. Let $\hat{i}_s(k^-)$ and $\hat{i}_s(k^+)$ denote the left and right limits of $\hat{i}_s(k)$, then according to Fig. 4, we have

$$\begin{cases} \hat{i}_s(k^-) = -(m_1+m_c)\hat{d}(k)T_s \\ \hat{i}_s(k^+) = (m_2-m_c)\hat{d}(k)T_s. \end{cases} \tag{3}$$

According to the Dirichlet conditions, $\hat{i}_s(k)$ is

$$\hat{i}_s(k) = \left(\hat{i}_s(k^-)+\hat{i}_s(k^+)\right)\Big/2. \tag{4}$$

Substituting (3) into (4), and then according to (2), we have

$$F_m = \frac{1}{\left[(m_1-m_2)/2+m_c\right]T_s}. \tag{5}$$

From the perspective of small signal analysis, the modulator can be regarded as an ideal sampler, and a series of narrow pulse signals in $\hat{d}$ can be treated as an impulse train, which is the sampling signal of the input signal $\hat{i}_s$ of the modulator. That is, the relationship between $\hat{d}$ and $\hat{i}_s$ can be expressed as

$$\hat{d}(t) = \sum_{n=-\infty}^{+\infty} \hat{d}(k)T_s = -F_m T_s \hat{i}_s(t) \sum_{n=-\infty}^{+\infty} \delta(t-kT_s) \tag{6}$$

where $\delta(t)$ is the Dirac delta function.

Due to the sampling characteristics of the modulator, if the converter initially has an ac small signal component at frequency ω_p, both $\hat{d}$ and $\hat{i}_s$ will contain ac components at $\omega_p+n\omega_s$ ($n\in\mathbb{Z}$). According to Shannon's sampling theorem, we have

$$\hat{d}(j\omega_p) = \hat{d}(j\omega_p+jn\omega_s) = -F_m \sum_{n=-\infty}^{+\infty} \hat{i}_s(j\omega_p+jn\omega_s). \tag{7}$$

According to (7) and defining $G_{\rm id}(s)$ as the transfer function from d to i_L, the control block diagram for the PCM controlled buck converter is depicted, as shown in Fig. 5. Hence, $G_{\rm PWM}(s)$ can be expressed as

$$\begin{aligned} &G_{\rm PWM}(s)\big|_{s=j\omega_p} \\ &= -\frac{\hat{d}(s)}{\hat{i}_s(s)} = \frac{F_m}{1+F_m H_i \sum\limits_{\substack{n=-\infty \\ n\neq 0}}^{+\infty} G_{\rm id}(s+jn\omega_s)}. \end{aligned} \tag{8}$$

Thus, the loop gain $T_i(s)$ can be written as

$$T_{\rm i}(s) = H_{\rm i} G_{\rm id}(s) G_{\rm PWM}(s). \tag{9}$$

Similarly, for VCM, the transfer functions of the modulator and the loop gain can also be derived, and they are the same as (8) and (9), and the control block diagram is still in the form of Fig. 5, except that the expression of F_m is changed to

$$F_m = \frac{1}{\left[(m_2-m_1)/2+m_c\right]T_s}. \tag{10}$$

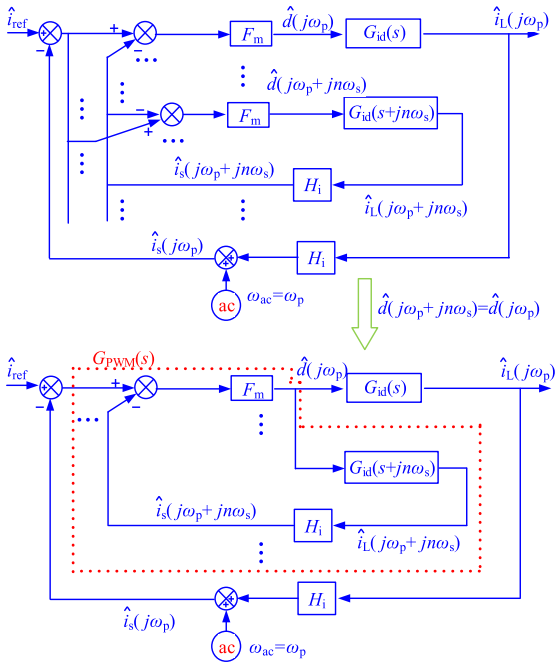

Fig. 5. Control block diagram of a PCM controlled buck converter.

C. Model Simplification

As seen from (8), $G_{\mathrm{PWM}}(s)$ contains infinite-term sideband components, thus hindering the stability analysis. So, (8) will be simplified and approximated with the example of a PCM controlled buck converter. The expression of $G_{\mathrm{id}}(s)$ of the buck converter is [40], [41]

$$G_{\mathrm{id}}(s)=\frac{V_{\mathrm{in}}\left(C_f s+1/R_{\mathrm{Ld}}\right)}{L_f C_f s^2+\left(L_f/R_{\mathrm{Ld}}+R_c C_f\right)s+1}. \tag{11}$$

At the frequencies higher than the resonance frequency of L_f and C_f, represented by f_r, $G_{\mathrm{id}}(s)$ can be expressed as [18]

$$G_{\mathrm{id\_}a}(s)=\frac{1}{H_i}\frac{m_1+m_2}{s}. \tag{12}$$

It can be found from (8) that, only at the frequencies close to nf_s ($n=\pm1, \pm2, \ldots$), the frequency response of the modulator is related to the low-frequency characteristic of $G_{\mathrm{id}}(s)$. Since f_r is usually much lower than f_s, it is reasonable to replace $G_{\mathrm{id}}(s)$ with $G_{\mathrm{id\_}a}(s)$. Substituting (12) into (8), and using the following series equality [42]:

$$\sum_{n=-\infty}^{+\infty}\frac{1}{n+x}=\pi\cot(\pi x)\quad(n\in\mathbb{Z},\ x\neq 0) \tag{13}$$

$G_{\mathrm{PWM}}(s)$ can be simplified as

$$G_{\mathrm{PWM\_a}}(s)=F_m\frac{1}{1+F_m H_i\sum_{\substack{n=-\infty\\ n\neq 0}}^{+\infty}G_{\mathrm{id\_}a}(s+jn\omega_s)}$$

$$=F_m\frac{1}{1+F_m\left(m_1+m_2\right)\left(\frac{1}{j\omega_s}\left(\sum_{n=-\infty}^{+\infty}\frac{1}{s/j\omega_s+n}\right)-\frac{1}{s}\right)}$$

$$=F_m\frac{1}{1+F_m(m_1+m_2)\left(\frac{\pi}{j\omega_s}\cot\left(\pi\frac{s}{j\omega_s}\right)-\frac{1}{s}\right)}. \tag{14}$$

Correspondingly, $T_i(s)$ is approximated to

$$T_{i\_a}(s)=H_i G_{\mathrm{id}}(s)G_{\mathrm{PWM\_}a}(s). \tag{15}$$

D. Stability Analysis

As seen from (14) and (15), the sideband components affect the converter stability through the modulator, which will be further illustrated in detail below by taking PCM as an example. First, defining the item related to "s" in the denominator of (14) as G_1(s), and at frequencies below $0.5f_s$, we have [43]

$$G_1(s)=\frac{\pi}{j\omega_s}\cot\left(\pi\frac{s}{j\omega_s}\right)-\frac{1}{s}\approx\frac{1}{s}+\frac{1}{3}s\frac{\pi^2}{{\omega_s}^2}-\frac{1}{s}=\frac{s}{3}\frac{\pi^2}{{\omega_s}^2}. \tag{16}$$

Substituting (16) into (14), $G_{\mathrm{PWM}}(s)$ below $0.5f_s$ can be written as

$$G_{\mathrm{PWM\_}a}(s)\approx\frac{F_m}{1+F_m(m_1+m_2)\frac{s}{3}\frac{\pi^2}{{\omega_s}^2}}. \tag{17}$$

As seen from (17), the dc gain of the modulator is F_m, and $G_{\mathrm{PWM}}(s)$ has a left-half-plane pole when $F_m>0$. The value of F_m corresponding to the PCM controlled buck converter in Table II is calculated to be 2.22 according to (5), which is the same as the ratio of $\hat{d}(2\,\mathrm{kHz})$ to $\hat{i}_s(2\,\mathrm{kHz})$ shown in Fig. 3, thus verifying the correctness of the derivation method for F_m. As seen from Fig. 3, when $f_p=2$ kHz ($\omega_p=2\pi f_p$), the amplitude of $\hat{i}_s$ at 102 and 98 kHz cannot be ignored. This means that the sideband components should also have a significant impact on the low-frequency characteristics of the modulator. The reason why the low-frequency gain of $G_{\mathrm{PWM}}(s)$ is still equal to F_m is that when $\omega_p << \omega_s$, $\omega_p \pm n\omega_s$ ($n=\pm1, \pm2, \ldots$) can be approximated as $\pm n\omega_s$, then the effect of $\hat{i}_s(j\omega_p+jn\omega_s)$ and $\hat{i}_s(j\omega_p-jn\omega_s)$ on $\hat{d}(j\omega_p)$ cancel each other out ($G_{\mathrm{id\_}a}(jn\omega_s)+G_{\mathrm{id\_}a}(-jn\omega_s)=0$).

In addition, it can be inferred from (11), (14), and (15) that, when $F_m>0$, the phase of $G_{\mathrm{PWM}}(s)$ in the entire frequency range is above –90° and the phase of $T_{\mathrm{i\_}a}(s)$ is greater than –180°, thus predicting the stability operation when m_c satisfies

$$m_c>\left(m_2-m_1\right)/2. \tag{18}$$

Moreover, according to (12), (14), and (15), it can be found that, if $m_c=0$, then at $0.5f_s$

$$T_{\mathrm{i\_}a}(s)\Big|_{s=\frac{1}{2}j\omega_s}\approx H_i G_{\mathrm{id\_}a}(s)G_{\mathrm{PWM\_}a}(s)\Big|_{s=\frac{1}{2}j\omega_s}$$
$$=\frac{F_m(m_1+m_2)/s}{1-F_m(m_1+m_2)/s}\Big|_{s=\frac{1}{2}j\omega_s}=\frac{2}{(1-2D)\pi j-2} \tag{19}$$

where D represents the duty cycle at steady state and $m_1D=m_2(1-D)$. As shown in (19), $T_{\mathrm{i\_}a}(j0.5\omega_s)$ is equal to -1 when $D=0.5$, thus predicting the phenomenon of subharmonic oscillation when D is larger than and close to 0.5.

E. Comparison and Simulation Verification

Table III presents the proposed model and the existing models in [18], [19], [29], and [35] for the PCM controlled buck converter, where $T_c(s)$ represents the closed-loop gain i.e., the

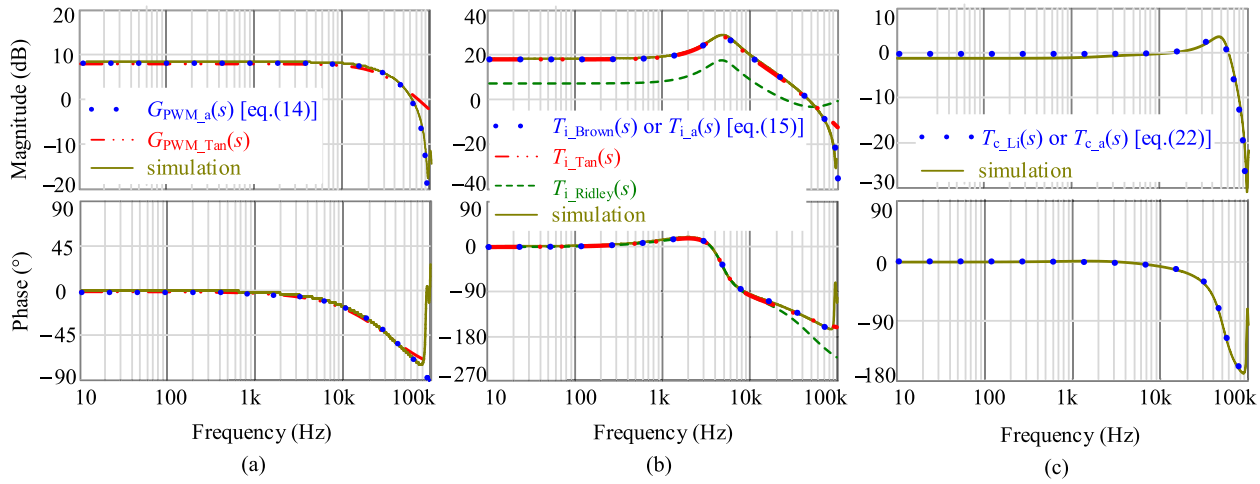

Fig. 6. Comparison between the theoretical models and the simulation results for a PCM controlled buck converter. (a) $G_{\rm PWM}$. (b) T_i. (c) T_c.

transfer function from $i_{\rm ref}$ to i_s. It is worth to point out that [29] only derived $T_c(s)$ by using the describing function method, and open-loop transfer function is not provided in Table III. Fig. 6 compares the Bode plots of $G_{\rm PWM}(s)$, $T_i(s)$, and $T_c(s)$ from different models with the simulated results with the circuit parameters in Table II, where $T_{i\_\rm Ridley}(s)$, $T_{i\_\rm Tan}(s)$, and $T_{i\_\rm Brown}(s)$ represent the expressions of $T_i(s)$ given in [18], [19], and [35], respectively. As can be seen from Fig. 6, the proposed models given by (14) and (15) are in good agreement with the simulated result in the entire frequency range, $T_{i\_\rm Tan}(s)$ is valid up to $0.5f_s$, and there is a clear distinction between $T_{i\_\rm Ridley}(s)$ and the simulated results. An explanation for Fig. 6 is made below.

In [35], a small delay ε ($\varepsilon \to 0^+$) is included in the modulator path and $G_{\rm id}(s)$ is replaced by $G_{\rm id\_}a(s)$ in the derivation process. Note that the final results given by $T_{i\_\rm Brown}(s)$ are different in the two cases when $\varepsilon \neq 0$ and $\varepsilon = 0$. Although the expressions of F_m given in [35] and this article are different, the final expressions of $T_i(s)$ are the same, which is further explained in Appendix I. Through exploring the physical concept of the small delay introduced in [35], we found two other methods to derive $G_{\rm PWM}(s)$ for PCM, and one of which is based on the minus ratio of $\hat{i}_s(k^-)$ and $\hat{d}(k)$, denoted by F_m^-, and the other uses the minus ratio of $\hat{i}_s(k^+)$ and $\hat{d}(k)$, denoted by F_m^+. Both methods introduce a delay or an advance item ε, and the obtained models are the same as that given by (14). These two methods are illustrated in Appendix I.

Both [18] and [19] first derive the relationship between $\hat{i}_{\rm ref}$ and $\hat{i}_s$ in the z-domain and then obtain the $T_c(s)$ by converting $\hat{i}_{\rm ref}$ and $\hat{i}_s$ into the s-domain with the following relationships (see (4.5) and (4.6) in [19]):

$$\hat{i}_s(s)=\frac{1-e^{-sT_s}}{s}\hat{i}_s(z)\,|_{z=e^{sT_s}}\ ,\quad \hat{i}_{\rm ref}(s)=T_s\hat{i}_{\rm ref}(z)\,|_{z=e^{sT_s}}\ . \tag{20}$$

Note that a zero-order-holder link $(1-e^{-sT_s})/s$ is introduced when obtaining $\hat{i}_s(s)$. However, the prerequisite for introducing this component is that $\hat{i}_s$ needs to remain unchanged over a switching cycle, and this condition holds only in general at high frequencies ($f_p > f_r$). This is because the capacitive reactance of C_f would be much smaller than the inductive reactance of L_f when $f_p > f_r$, consequently, the slope of the inductor current during the ON-time and OFF-time of the switch can be approximated as $(V_{\rm in}-V_o)/L_f$ and $-V_o/L_f$, respectively (same as that at steady state), by neglecting the output voltage perturbation $\hat{v}_o$, which makes $\hat{i}_s$ a constant over a switching period. If $f_p < f_r$, then $\hat{v}_o$ will have an unignorable effect on the slope of the inductor current, therefore, in this case, $\hat{i}_s$ is no longer a constant, which also can be inferred from the waveforms shown in Fig. 3.

According to Fig. 2, $T_c(s)$ can be readily derived as

$$T_c(s)=\frac{T_i(s)}{1+T_i(s)}=\frac{H_iF_mG_{\rm id}(s)}{1+H_iF_m\sum_{n=-\infty}^{+\infty}G_{\rm id}(s+jn\omega_s)}. \tag{21}$$

By replacing $G_{\rm id}(s)$ in (21) with $G_{\rm id\_}a(s)$, $T_c(s)$ at frequencies higher than f_r can be simplified as

$$\begin{aligned}T_{c\_a}(s)&\approx\frac{H_iF_mG_{\rm id\_}a(s)}{1+H_iF_m\sum_{n=-\infty}^{+\infty}{\rm G}_{\rm id\_}a(s+jn\omega_s)}\\&=\frac{1-\alpha}{1-\alpha e^{-sT_s}}\frac{1-e^{-sT_s}}{sT_s}\end{aligned} \tag{22}$$

where the expression of α can been found in Table III, which is the same as that given in [18], [19], and [29], implying the $T_c(s)$ obtained in [18], [19], and [29] is only a special case of the result obtained in this article.

The expressions of $T_i(s)$ in [18] and [19] are further extracted based on $T_c(s)$. In [18], $T_{i\_\rm Ridley}(s)$ was solved from

$$\begin{aligned}T_{c\_a}(s)&=\frac{1-\alpha}{1-\alpha e^{-sT_s}}\frac{1-e^{-sT_s}}{sT_s}=\frac{H_iF_mG_{\rm id}(s)}{1+T_{i\_\rm Ridley}(s)}\\&=\frac{H_iF_mG_{\rm id}(s)}{1+H_iF_mG_{\rm id}(s)H_e(s)}\approx\frac{H_iF_mG_{\rm id\_}a(s)}{1+H_iF_mG_{\rm id\_}a(s)H_e(s)}\end{aligned} \tag{23}$$

which introduced an additional gain block $H_e(s)$ (see (3.14) in [18]) into the feedback path, but lacks a solid theoretical basis. Besides, the expression of F_m in [18] is also incorrect. So $T_{i\_\rm Ridley}(s)$ exhibits very low accuracy in the entire frequency range, as observed in Fig. 6(b).

TABLE III
COMPARISON OF THE EXISTING MODELS AND THE RESULTS OBTAINED IN THIS ARTICLE

	$F_{\rm m}$	$G_{\rm PWM}(s)$	$T_{\rm i}(s)$	$T_{\rm c}(s)$
Ridley's Model [18]	$\frac{1}{(m_1+m_{\rm c})T_{\rm s}}$	—	$F_{\rm m}H_{\rm i}G_{\rm id}(s)H_{\rm e}(s)$	$\frac{1-\alpha}{1-\alpha e^{-sT_{\rm s}}}\frac{1-e^{-sT_{\rm s}}}{sT_{\rm s}}$
Tan's Model [19]	$\frac{1}{\left(\frac{m_1-m_2}{2}+m_{\rm c}\right)T_{\rm s}}$	$\frac{F_m}{1+\frac{4F_{\rm m}(m_1+m_2)s}{\omega_{\rm s}^2}}$	$\frac{F_{\rm m}H_{\rm i}G_{\rm id}(s)}{1+\frac{4F_{\rm m}(m_1+m_2)s}{\omega_{\rm s}^2}}$	$\frac{1-\alpha}{1-\alpha e^{-sT_{\rm s}}}\frac{1-e^{-sT_{\rm s}}}{sT_{\rm s}}$
Li Jian's Model [29]	—	—	—	$\frac{1-\alpha}{1-\alpha e^{-sT_{\rm s}}}\frac{1-e^{-sT_{\rm s}}}{sT_{\rm s}}$
Brown's Model [35]	$\frac{1}{(m_1+m_{\rm c})T_{\rm s}}$	—	$\frac{F_{\rm m}H_{\rm i}G_{\rm id}(s)}{1+F_{\rm m}H_{\rm i}\sum_{\substack{n=-\infty\\ n\neq 0}}^{+\infty}G_{\rm id\_a}(s+jn\omega_{\rm s})e^{-(s+jn\omega_{\rm s})\varepsilon}}$	—
The model in this paper	$\frac{1}{\left(\frac{m_1-m_2}{2}+m_{\rm c}\right)T_{\rm s}}$	$\frac{F_{\rm m}}{1+F_{\rm m}H_{\rm i}\sum_{\substack{n=-\infty\\ n\neq 0}}^{+\infty}G_{\rm id}(s+jn\omega_{\rm s})}$	$\frac{F_{\rm m}H_{\rm i}G_{\rm id}(s)}{1+F_{\rm m}H_{\rm i}\sum_{\substack{n=-\infty\\ n\neq 0}}^{+\infty}G_{\rm id}(s+jn\omega_{\rm s})}$	$\frac{F_{\rm m}H_{\rm i}G_{\rm id}(s)}{1+F_{\rm m}H_{\rm i}\sum_{n=-\infty}^{+\infty}G_{\rm id}(s+jn\omega_{\rm s})}$

Note: 1. $H_{\rm e}(s)=\frac{sT_s}{e^{sT_s}-1}\approx 1-\frac{1}{2/\pi}\frac{s}{\omega_s 2}+(\frac{s}{\omega_s 2})^2$ 2. $\alpha=-\frac{m_2-m_c}{m_1+m_c}$ 3. "—" represents the result was not given.
4. In this table, the expression of $T_{i\_\rm Tan}$ is given based on the actual expression used in the verification process in [19], rather than the original expression in (25).

In [19], $T_{i\_\rm Tan}(s)$ was obtained from

$$T_{c\_a}(s)=\frac{1-\alpha}{1-\alpha e^{-sT_s}}\frac{1-e^{-sT_s}}{sT_s}=\frac{T_{i\_\rm Tan}(s)}{1+T_{i\_\rm Tan}(s)} \tag{24}$$

and expressed as

$$T_{i\_\rm Tan}(s)\approx\frac{\frac{m_1+m_2}{s[(m_2-m_1)/2+m_c]T_s}}{1+\frac{4(m_1+m_2)S}{\omega_s^2[(m_2-m_1)/2+m_c]T_s}}=\frac{F_{\rm m}H_{\rm i}G_{\rm id\_a}(s)}{1+\frac{4F_m(m_1+m_2)S}{\omega_s^2}}. \tag{25}$$

Based on this, the resultant transfer function from d to i_L in $T_{i\_\rm Tan}(s)$ is $G_{\rm id\_a}(s)$, meaning $T_{i\_\rm Tan}(s)$ is accurate only at frequencies higher than f_r. However, [19] replaced $G_{\rm id\_a}(s)$ in $T_{i\_\rm Tan}(s)$ with $G_{\rm id}(s)$ in the process of experimental verification without justification. Although this modification improved the accuracy of $T_{i\_\rm Tan}(s)$, as confirmed in Fig. 6(b), the modeling method is not very well-founded especially in the low-frequency range.

It should be mentioned that the low-frequency gains of $T_i(s)$ from the aforementioned models are all much greater than 1, thus the low-frequency gain of $T_c(s)$ is pretty close to 1, which suggests that the good agreement between the theoretical model (22) and the actual response cannot tell the validity of the modeling method at low frequencies. In conclusion, the modeling methods proposed in [18], [19], and [29] are invalid at low frequencies due to the assumption that $\hat{i}_s$ remains unchanged during a switching cycle when deriving the expression of $T_c(s)$.

III. SAMPLED-DATA MODELING FOR PVM/VVM

In this section, the small-signal models of the PVM/VVM controlled buck converter will be derived and then simplified by using the same methodology for the PCM/VCM control.

A. Sampled-Data Modeling

Fig. 7 shows the circuit diagram of a PVM/VVM controlled buck converter and the representations of the variables are the same as those shown in Fig. 2. Besides, i_c is the current flowing through the output capacitor, v_o, v_c, and $v_{\rm fb}$ are the output voltage, the voltage of C_f, and the voltage feedback, respectively, H_v is the voltage sensor gain, implemented by the divider consists of resistors R_1 and R_2. Next, PVM will be taken as an example to derive the small-signal models.

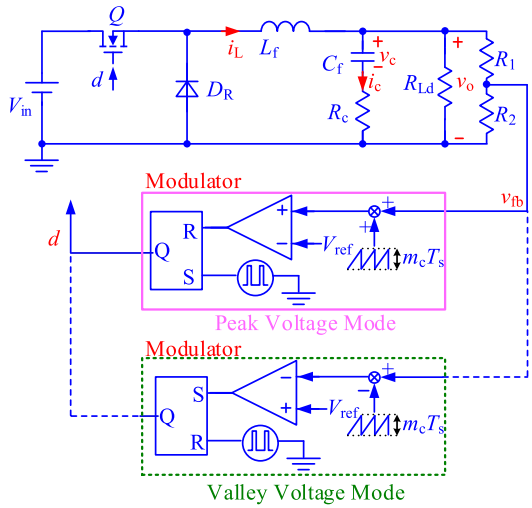

Fig. 7. PVM/VVM controlled buck converter.

Similar to the PCM control, in the PVM control, the definitions of the transfer function of the modulator $G_{\rm PWM}(s)$ and the modulator gain factor F_m are similar to those in (1) and (2), respectively, while $\hat{i}_s$ should be replaced by $\hat{v}_{\rm fb}$.

Figs. 8 and 9 show the operating principle of the modulator at steady state and perturbated state, respectively, where the sampling instant is selected as the beginning time in each cycle. In Fig. 8, m_1 and $-m_2$ are the respective slopes of i_L during the switch ON-time and OFF-time, $m_{\rm cf}$ is the slope of v_c at the sampling instant, $v'_{\rm fb}(k^-)$ and $v'_{\rm fb}(k^+)$ are the left and right limits of the slope of $v_{\rm fb}$ at kT_s, respectively. In Fig. 9, $\hat{v}_{\rm fb}$ and $\hat{d}$ denote the perturbation signal in $v_{\rm fb}$ and d, respectively, $\hat{v}_{\rm fb}(k^-)$,

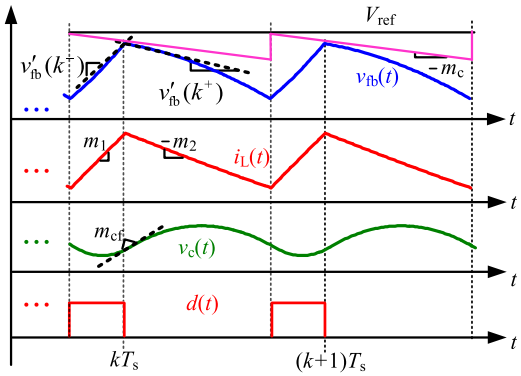

Fig. 8. Key waveforms of a PVM controlled buck converter at steady state.

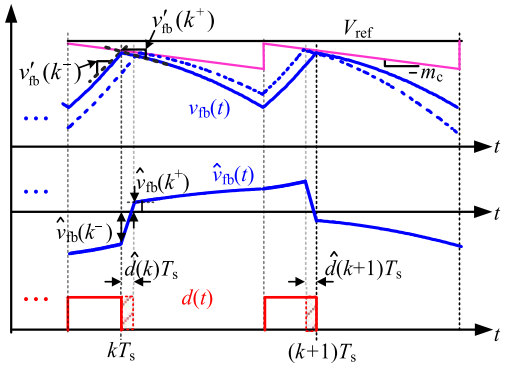

Fig. 9. Key waveforms of the circuit shown in Fig. 7 in the perturbed state.

$\hat{v}_{\rm fb}(k^+)$, and $\hat{d}(k)$ are the left and right limits of $\hat{v}_{\rm fb}$, and the value of $\hat{d}$ at kT_s, respectively.

Defining the value of $\hat{v}_{\rm fb}$ at kT_s as $\hat{v}_{\rm fb}(k)$, and using the same principle as mentioned in Section II, one can find that

$$\hat{v}_{\rm fb}(k) = \left(\hat{v}_{\rm fb}(k^-) + \hat{v}_{\rm fb}(k^+)\right)/2. \tag{26}$$

From Figs. 8 and 9, we have

$$\begin{cases} \hat{v}_{\rm fb}(k^-) = -\left(v'_{\rm fb}(k^-) + m_c\right)\hat{d}(k)T_s \\ \hat{v}_{\rm fb}(k^+) = \left(-v'_{\rm fb}(k^+) - m_c\right)\hat{d}(k)T_s. \end{cases} \tag{27}$$

From Figs. 7 and 8, $m_{\rm cf}$ can be obtained as

$$\begin{aligned} m_{\rm cf} &= \frac{dv_C}{dt}\,|_{t=kT_s} = \frac{i_c(t)}{C_f}\,|_{t=kT_s} \approx \frac{i_L(t)-I_o}{C_f}\,|_{t=kT_s} \\ &= \frac{m_1 DT_s}{2C_f} \end{aligned} \tag{28}$$

where I_o is the load current, and note this equation is derived at steady state. According to Figs. 7 and 8, and (28), the expressions of $v'_{\rm fb}(k^-)$ and $v'_{\rm fb}(k^+)$ can be derived as

$$\begin{cases} v'_{\rm fb}(k^-) = H_v\left(R_c m_1 + m_{\rm cf}\right) = H_v\left(R_c m_1 + \frac{m_1 DT_s}{2C_f}\right) \\ v'_{\rm fb}(k^+) = H_v\left(-R_c m_2 + m_{\rm cf}\right) = H_v\left(-R_c m_2 + \frac{m_1 DT_s}{2C_f}\right) \end{cases} \tag{29}$$

where

$$H_v = \frac{R_2}{R_1 + R_2}. \tag{30}$$

Substituting (29) into (27), then according to (26) and the definition of F_m, we have

$$F_m = \frac{1}{H_v\left(R_c\frac{m_1-m_2}{2} + \frac{m_1 DT_s}{2C_f}\right)T_s + m_c T_s}. \tag{31}$$

Using the same method, it can be found that for VVM

$$F_m = \frac{1}{H_v\left(R_c\frac{m_2-m_1}{2} + \frac{m_1 DT_s}{2C_f}\right)T_s + m_c T_s}. \tag{32}$$

Furthermore, using the same derivation process mentioned in Section II, $G_{\rm PWM}(s)$ can be expressed as

$$G_{\rm PWM}(s) = \frac{F_m}{1 + F_m H_v \sum_{\substack{n=-\infty \\ n\neq 0}}^{+\infty} G_{\rm vd}(s + jn\omega_s)} \tag{33}$$

where $G_{\rm vd}(s)$ is the transfer function from d to v_o. For buck converter, it is expressed as [40], [41]

$$G_{\rm vd}(s) = V_{\rm in}\frac{R_c C_f s + 1}{L_f C_f s^2 + \left(L_f/R_{\rm Ld} + R_c C_f\right)s + 1}. \tag{34}$$

Finally, the loop gain T_v(s) is given as

$$T_v(s) = H_v G_{\rm vd}(s) G_{\rm PWM}(s). \tag{35}$$

B. Model Simplification

It is difficult to analyze the stability by using the model given by (33) since it contains infinite-term sideband components. Given $G_{\rm vd}(s)$ decreases with a slope of –40 dB/dec at high frequencies, it only needs to consider the finite sideband components. Defining $G_{\rm PWM\_M}(s)$ and $T_{v\_M}(s)$ as the transfer function of the modulator and the loop gain which include only the components within M multiples of the switching frequency range, i.e.,

$$G_{\rm PWM\_M}(s) = \frac{F_m}{1 + F_m H_v \sum_{\substack{n=-M \\ n\neq 0}}^{+M} G_{\rm vd}(s + jn\omega_s)} \tag{36}$$

$$T_{v\_M}(s) = H_v G_{\rm vd}(s) G_{\rm PWM\_M}(s). \tag{37}$$

For example, if M is selected as 1, $G_{\rm PWM\_1}(s)$ and $T_{v\_1}(s)$, respectively, represent $G_{\rm PWM}(s)$ and $T_v(s)$, which only include the sideband components around the switching frequency. Another approximation method is similar to that mentioned in Section II. When $s > 2\pi f_r$, $G_{\rm vd}(s)$ can be simplified to $G_{\rm vd\_a}(s)$ expressed as

$$G_{\rm vd\_a}(s) = V_{\rm in}\frac{R_c C_f s + 1}{L_f C_f s^2} = \frac{V_{\rm in}}{L_f C_f}\left(\frac{R_c C_f}{s} + \frac{1}{s^2}\right). \tag{38}$$

By substituting (38) into (33), the approximations of $G_{\rm PWM}(s)$ and $T_v(s)$, denoted as $G_{\rm PWM\_a}(s)$ and $T_{v\_a}(s)$, respectively, will be valid at all frequencies except for a small range near the multiples of the switching frequency. Furthermore, using the following infinite sum formulas [42]:

$$\begin{cases} \sum_{k=-\infty}^{+\infty}\frac{1}{k+x} = \pi\cot(\pi x) \\ \sum_{k=-\infty}^{+\infty}\frac{1}{(k+x)^2} = \frac{\pi^2}{\sin^2(\pi x)} \end{cases} (k\in\mathbb{Z},\ x\neq 0) \tag{39}$$

the expressions of $G_{\mathrm{PWM\_}a}(s)$ and $T_{v\_a}(s)$ can be further simplified to the results as expressed in (40) and (41), shown at the bottom of this page, respectively.

C. Stability Analysis

Same as the PCM control, it can be found from (40) and (41), the sideband components affect the converter stability through the modulator in the PVM/VVM control, which will be further illustrated in detail below with the example of a PVM controlled buck converter. First, the influence of the sideband components on the low-frequency gain of the modulator is analyzed. Defining the term related to "$\sin(\pi s/j\omega_s)$" in the denominator of (40) as $G_2(s)$, and at frequencies below $0.3f_s$, we have [44]

$$G_2(s) = \frac{1}{(j\omega_s)^2}\frac{\pi^2}{\sin^2(\pi s/j\omega_s)} - \frac{1}{s^2} \approx -\frac{1}{3}\frac{\pi^2}{{\omega_s}^2}. \tag{42}$$

Another term related to "$\cot(\pi s/j\omega_s)$" in (40) has been given in (16). Therefore, combining (16), (40), and (42), at frequencies below $0.3f_s$, (40) can be rewritten as

$$G_{\mathrm{PWM\_}a}(s) \approx \frac{F_m}{1+\frac{F_m H_v V_{\mathrm{in}}}{L_f C_f}\left(-\frac{1}{3}\frac{\pi^2}{{\omega_s}^2} + R_c C_f \frac{s}{3}\frac{\pi^2}{{\omega_s}^2}\right)}. \tag{43}$$

As seen from (43), the low-frequency gain of the modulator equals to $F_m/(1 - \frac{F_m H_v V_{\mathrm{in}}}{L_f C_f}\frac{1}{3}\frac{\pi^2}{{\omega_s}^2})$, rather than F_m, due to the sideband effect.

Furthermore, since the amplitude of $G_1(s)$ and $G_2(s)$ become larger as frequency increases, and the phase of $G_1(s)$ is always 90°, the phase of $G_2(s)$ is always –180°. Therefore, it can be concluded that the sideband effect makes the amplitude and the phase of the frequency response of the modulator decrease as frequency increases in the high-frequency region. Also, it is well known that the phase of $G_{\mathrm{vd}}(s)$ alters in the range from –90° to –180° at frequencies higher than f_r, and the smaller the time constant of the output capacitor $C_f R_c$ is, the closer the phase of $G_{\mathrm{vd}}(s)$ is to –180°. Moreover, the phase of $G_{\mathrm{PWM}}(s)$ is negative in the high-frequency region. Hence, it can be inferred that a larger time constant $R_c C_f$ is preferred to ensure the converter stability.

Now, the condition under which a PVM controlled buck converter is stable is derived based on (38), (40), and (41). At $0.5f_s$, the loop gain is

$$\begin{aligned} T_{v\_a}(s)\Big|_{s=\frac{\omega_s j}{2}} &\approx H_v G_{\mathrm{vd\_}a}(s) G_{\mathrm{PWM\_}a}(s) \\ &= \frac{\frac{1}{s^2}+\frac{R_c C_f}{s}}{\frac{1}{a} - \frac{\pi^2}{{\omega_s}^2} - \frac{1}{s^2} - \frac{R_c C_f}{s}}\Bigg|_{s=\frac{\omega_s j}{2}} \end{aligned} \tag{44}$$

where

$$a = \frac{F_m H_v V_{\mathrm{in}}}{L_f C_f} = \frac{1}{\left(R_c C_f \frac{1-2D}{2} + \frac{(1-D)DT_s}{2}\right)T_s + \frac{m_c C_f T_s}{m_1+m_2}}. \tag{45}$$

According to (44), one can find that $T_{v\_a}(j0.5\omega_s) = -1$ when $1/a - \pi^2/{\omega_s}^2 = 0$, and the magnitude of $T_{v\_a}(j0.5\omega_s)$ is larger than 0 dB, the phase of $T_{v\_a}(j0.5\omega_s)$ is lower than –180° when $1/a - \pi^2/{\omega_s}^2 < 0$. Therefore, it can be inferred that a PVM controlled buck converter is stable when $1/a - \pi^2/{\omega_s}^2 > 0$, in which the magnitude of $T_{v\_a}(j0.5\omega_s)$ is less than 0 dB, the phase of $T_{v\_a}(j0.5\omega_s)$ is great than –180°. That is to say, for PVM, $R_c C_f$ or m_c needs to satisfy

$$\begin{cases} \frac{R_c C_f}{T_s} > \frac{1}{2} + \frac{D^2}{1-2D} \text{ and } D < \frac{1}{2} & (m_c = 0) \\ \frac{m_c L_f}{H_v V_{\mathrm{in}} R_c} > \frac{2D-1}{2} + \frac{T_s}{R_c C_f}\left(\frac{1-2D}{4} + \frac{D^2}{2}\right) \text{ and } D < \frac{1}{2} & (m_c \neq 0). \end{cases} \tag{46}$$

Similarly, with the same analysis, we can find that for VVM, $R_c C_f$ or m_c needs to satisfy

$$\begin{cases} \frac{R_c C_f}{T_s} > \frac{1}{2} + \frac{D'^2}{1-2D'} = -\frac{1}{2} + \frac{D^2}{2D-1} \text{ and } D > \frac{1}{2} & (m_c = 0) \\ \frac{m_c L_f}{H_v V_{\mathrm{in}} R_c} > \frac{2D'-1}{2} + \frac{T_s}{R_c C_f}\left(\frac{1-2D'}{4} + \frac{D'^2}{2}\right) \text{ and } D > \frac{1}{2} & (m_c \neq 0) \end{cases} \tag{47}$$

where D represents the duty cycle at steady state and $D' = 1 - D$. The results given by (46) and (47) are the same as those obtained in [6] by using the discrete modeling method (see (5)-(7) in [6]).

D. Comparison and Simulation Verification

In [29], the expression of the closed-loop gain $T_c(s)$ for the PVM controlled buck converter, i.e., the transfer function from v_{ref} to v_{fb}, represented by $T_{c\_\mathrm{Li}}(s)$ as given in Appendix II, was obtained by using the describing function method. In order to compare with $T_{c\_\mathrm{Li}}(s)$, the expressions of $T_c(s)$ in this article are derived by using $T_{v\_M}(s)$ and $T_{v\_a}(s)$, and the obtained results are denoted as $T_{c\_M}(s)$ and $T_{c\_a}(s)$, respectively, which are defined as

$$\begin{aligned} T_{c\_M}(s) &= \frac{T_{v\_M}(s)}{1 + T_{v\_M}(s)} \\ &= \frac{F_m H_v G_{\mathrm{vd}}(s)}{1 + F_m H_v \sum_{n=-M}^{+M} G_{\mathrm{vd}}(s + jn\omega_s)} \\ T_{c\_a}(s) &= \frac{T_{v\_a}(s)}{1 + T_{v\_a}(s)} \end{aligned} \tag{48}$$

$$G_{\mathrm{PWM\_}a}(s) = \frac{F_m}{1+F_m H_v \sum_{\substack{n=-\infty \\ n\neq 0}}^{+\infty} G_{\mathrm{vd\_}a}(s+jn\omega_s)} = \frac{F_m}{1+\frac{F_m H_v V_{\mathrm{in}}}{L_f C_f}\left(\frac{1}{(j\omega_s)^2}\frac{\pi^2}{\sin^2(\pi s/j\omega_s)} - \frac{1}{s^2}\right) + \frac{F_m H_v V_{\mathrm{in}}}{L_f C_f} R_c C_f \left(\frac{\pi}{j\omega_s}\cot\left(\pi\frac{s}{j\omega_s}\right) - \frac{1}{s}\right)} \tag{40}$$

$$T_{v\_a}(s) = H_v G_{\mathrm{vd}}(s) G_{\mathrm{PWM\_}a}(s) \tag{41}$$

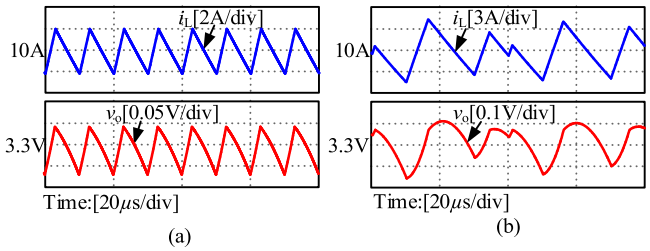

Fig. 10. Simulated waveforms with different C_f. (a) $C_f = 300$ μF. (b) $C_f = 100$ μF.

$$= \frac{F_m H_v G_{\mathrm{vd}}(s)}{1+F_m H_v \left(G_{\mathrm{vd}}(s)+\sum_{\substack{n=-\infty \\ n\neq 0}}^{+\infty} G_{\mathrm{vd\_}a}(s+jn\omega_s)\right)}. \tag{49}$$

It can be found that at frequencies higher than f_r, (49) can be further simplified as the following equation by replacing $G_{\mathrm{vd}}(s)$ with $G_{\mathrm{vd\_}a}(s)$ and substituting the expression of F_m into it:

$$T_{c\_a}(s) \approx \frac{F_m H_v G_{\mathrm{vd\_}a}(s)}{1 + F_m H_v \sum_{n=-\infty}^{+\infty} \mathrm{G}_{\mathrm{vd\_}a}(s + jn\omega_s)}$$

$$= \frac{G_{\mathrm{vd\_}a}(s)}{\frac{1}{F_m H_v} + \frac{m_1+m_2}{C_f}\left(\frac{R_c C_f \pi}{j\omega_s}\cot\left(\pi\frac{s}{j\omega_s}\right)+\frac{\pi^2/(j\omega_s)^2}{\sin^2(\pi s/j\omega_s)}\right)}. \tag{50}$$

It should be noted that $T_{c\_\mathrm{Li}}(s)$ can also be rearranged to the form in (50) without approximation, as proved in Appendix II. Similar to the scenario in the PCM control, the low-frequency gain of $T_c(s)$ is very close to 1 regardless of the expression of $G_{\mathrm{vd}}(s)$ in the PVM control, which suggests that the good agreement between the theoretical model (50) and the actual response cannot tell the validity of the modeling method at low frequencies.

To summarize, the modeling method proposed in [29] is invalid at low frequencies due to the introduction of the assumption that the perturbation signal in the voltage across the ESR of the output capacitor remains unchanged during a switching cycle into the derivation process of $T_c(s)$.

To demonstrate the correctness of the proposed models, a PVM controlled buck converter is simulated in Simplis software, and the circuit parameters are given in Table II except that $R_c = 30$ mΩ, $C_f = 300$ μF or 100 μF, $R_1 = 2.1$ kΩ, and $R_2 = 1.2$ kΩ.

Fig. 10 shows the simulated time-domain waveforms when different C_f are used. As seen, the converter is unstable when $C_f = 100$ μF, but turns stable when $C_f = 300$ μF, as predicted by (46). Figs. 11 and 12 show the Bode plots of the theoretical models and the simulated results when different C_f are used. As seen, the theoretical models represented by (40), (41), and (50) are in good agreement with the corresponding simulated results as expected. Also, it can be found that $G_{\mathrm{PWM\_1}}(s)$ and $T_{v\_1}(s)$ have deviations from the simulation results in the low-frequency range, which indirectly proves that the sideband effect could also affect the low-frequency response of the modulator.

Moreover, as seen from Fig. 12(b), the cut-off frequency of the loop gain is close to $0.5f_s$ and the phase margin is negative, thus predicting the instability phenomenon which matches the case demonstrated in Fig. 10(b).

IV. Extension of the Sampled-Data Modeling to Other Topologies

The proposed modeling method in Section II can also be applied to the PCM/VCM controlled boost/buck–boost converter. For the boost/buck–boost converter, the $G_{\mathrm{id}}(s)$ derived with the average technique, represented by $G_{\mathrm{id\_av}}(s)$, is inaccurate within a small range close to nf_s ($n = \pm 1, \pm 2, \ldots$), which means that the $G_{\mathrm{PWM\_}a}(s)$ in (14) is invalid in the low-frequency range. Fortunately, an exact $G_{\mathrm{id}}(s)$ can be derived by using the describing function modeling method [45], [46], denoted as $G_{\mathrm{id\_DF}}(s)$ here. Substituting $G_{\mathrm{id\_DF}}(s)$ into (8) leads to the $G_{\mathrm{PWM\_DF}}(s)$, which can accurately describe the frequency response of the modulator.

Fig. 13 makes a comparison of the theoretical models with the simulated results for a PCM controlled boost converter, where $G_{\mathrm{PWM\_DF\cdot 1}}(s)$ represents the result when only the sideband components around f_s are considered for $G_{\mathrm{PWM\_DF}}(s)$. The parameters of the boost converter are as follows: $V_{\mathrm{in}} = 48$ V, $V_o = 80$ V, $R_{\mathrm{Ld}} = 12.8$ Ω, $L_{\mathrm{f}} = 95$ μH, $C_f = 470$ μF, $R_c = 47$ mΩ, $H_{\mathrm{i}} = 0.1$, and $f_s = 100$ kHz. The resonance frequency f_r can be calculated as 450 Hz.

For the boost/buck–boost converter with the PVM/VVM control, if the ESR of the output capacitor is small, then the sampled-data modeling proposed in Section III is still applicable as long as the accurate $G_{\mathrm{vd}}(s)$ in [45], [46] is used, which is the same as that in the PCM/VCM controlled boost/buck–boost converter. However, if the ESR of the output capacitor is large, the situation of $\hat{v}_{\mathrm{fb}}$ will have a step up (for PVM) or a step down (for VVM) at each sampling instant, making it much more complicated than a discontinuity of the first kind. Therefore, the modeling method proposed in Section III is not suitable for the PVM/VVM controlled boost/buck–boost converter with the large ESR of the output capacitor.

V. Experimental Verification

In order to verify the validity of the sampled-data modeling method proposed in this article, a PCM controlled buck converter prototype with the UC3824 controller and the INA293 current sense amplifier was fabricated in the lab, and the circuit parameters have been given in Table II. The Bode plot data were obtained by using the network analyzer Agilent E5061B and the analog signal injection method [19].

Fig. 14 shows the comparison of the proposed models with the experimental results when $m_c = 0$. It can be found that the models represented by (14) and (15) are in good agreement with the experimental results and are accurate in the entire switching frequency range except for a small difference at the frequencies close to f_s, verifying the correctness of the proposed models.

VI. Conclusion

This article developed a unified sampled data modeling method for ripple-based control schemes based on the sampling

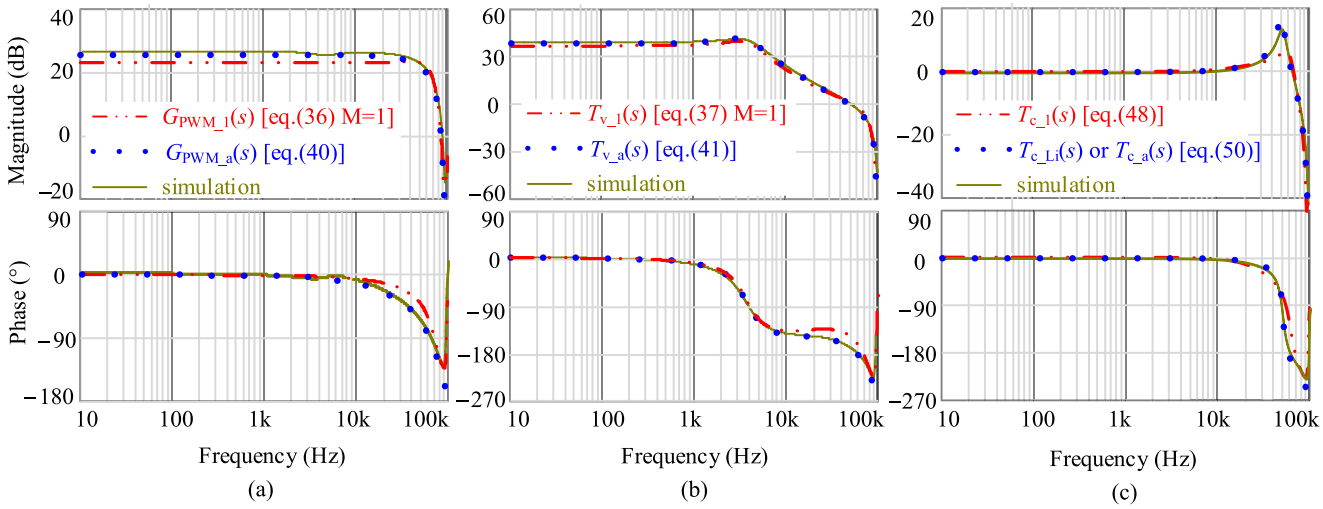

Fig. 11. Comparison between theoretical models and simulation results when $C_f = 300\ \mu$F. (a) $G_{\rm PWM}$. (b) T_v. (c) T_c.

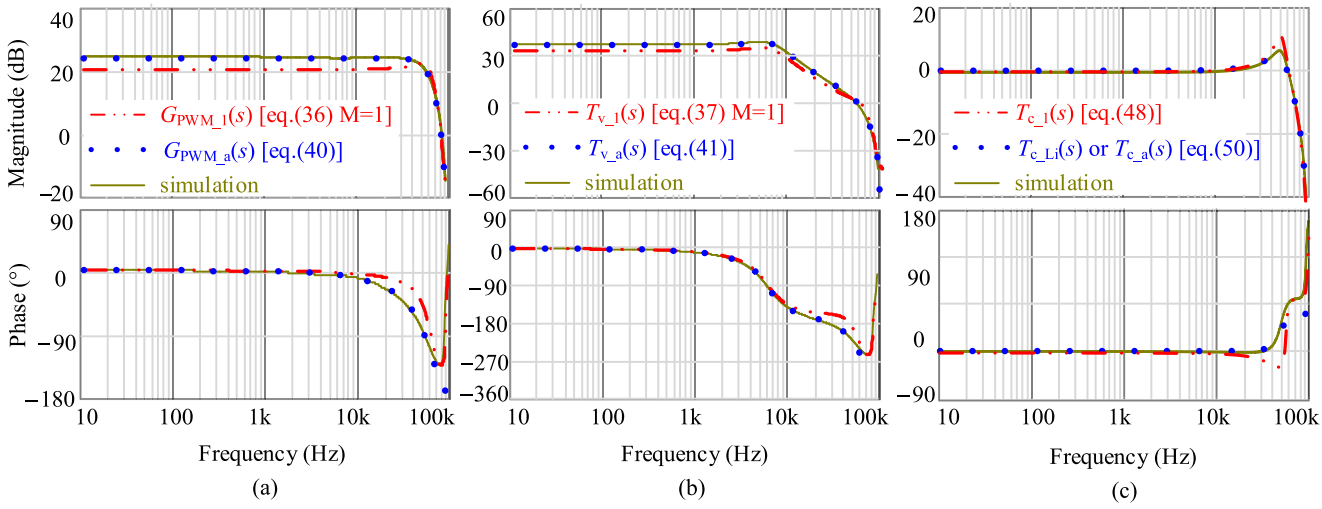

Fig. 12. Comparison between theoretical models and simulation results when $C_f = 100\ \mu$F. (a) $G_{\rm PWM}$. (b) T_v. (c) T_c.

characteristic of the modulator. It is divided into two parts, and in this first part, the models for PCM/VCM and PVM/VVM are derived. It is pointed out that the perturbation signal in the current feedback or voltage signal has a discontinuity of the first kind at the sampling instant. Consequently, when deriving the modulator gain factor F_m, the Dirichlet conditions must be satisfied, that is, the value of $\hat{i}_s$ or $\hat{v}_{\rm fb}$ should be equal to half of the sum of the limit values on the left and right sides of this signal at the sampling instant.

Based on the theoretical models of the buck converter with the PCM/VCM/PVM/VVM control, the effect of the sideband components on the converter stability is analyzed, and the stability conditions are determined. Finally, simulation and experimental results verify the proposed models. The next part will present the sampled-data modeling method for constant ON-time control and constant OFF-time control.

APPENDIX I.

The research in this appendix is inspired by the result obtained by Brown [35]. Here, we present two other modeling methods to derive the $G_{\rm PWM}(s)$ for PCM as well as the verification of the equivalence between the expression of $T_{i\_\rm Brown}(s)$ and the result given by (15).

The core idea adopted in the derivation process in Section II is that the duty cycle perturbation signal $\hat{d}$ can be regarded as an impulse train, and $\hat{i}_s$ has a discontinuity of the first kind at each sampling instant, as depicted in Fig. 15, where $\varepsilon = kT_s - kT_s^- = kT_s^+ - kT_s$.

Letting $F_m^- = -\hat{d}(k)/\hat{i}_s(k^-)$ and $F_m^+ = -\hat{d}(k)/\hat{i}_s(k^+)$, then according to Figs. 3, 4, and 15, we have

$$\hat{d}(t) = \sum_{n=-\infty}^{+\infty} \hat{d}(k)T_s = -F_m^- T_s \hat{i}_s(t-\varepsilon) \sum_{n=-\infty}^{+\infty} \delta(t - kT_s) \tag{A1}$$

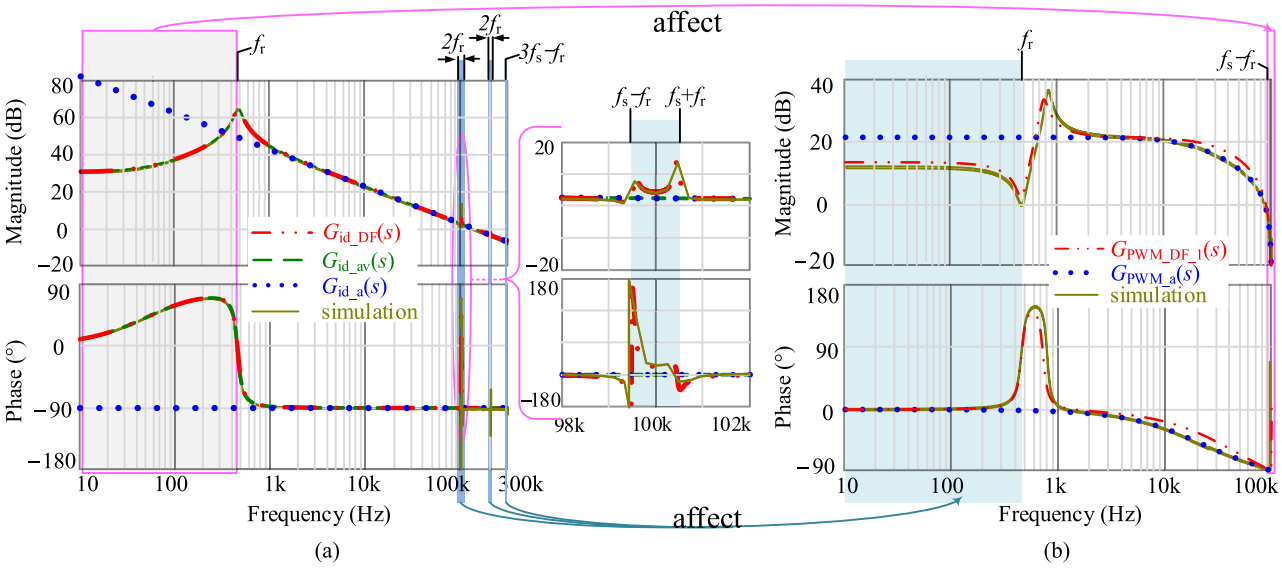

Fig. 13. Comparison between theoretical models and simulation results for a PCM controlled boost converter. (a) G_{id}. (b) G_{PWM}.

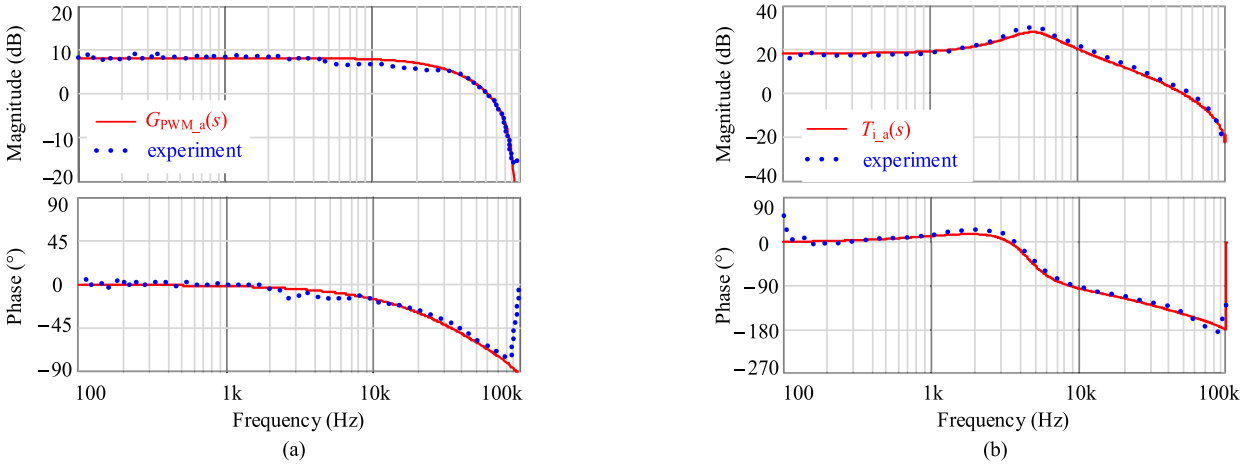

Fig. 14. Comparison between theoretical models and experimental measurements for a PCM controlled buck converter. (a) G_{PWM}. (b) T_i.

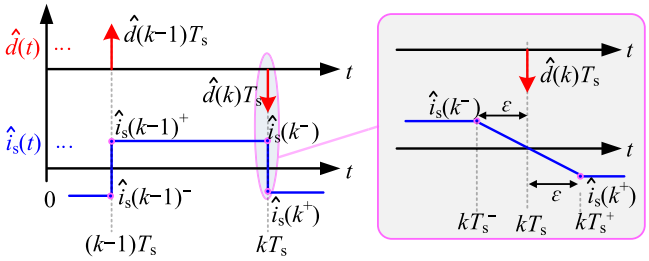

Fig. 15. Approximate waveforms of $\hat{d}$ and $\hat{i}_s$ under PCM control.

$$\hat{d}(t)=\sum_{n=-\infty}^{+\infty}\hat{d}(k)T_s=-F_m^+T_s\hat{i}_s(t+\varepsilon)\sum_{n=-\infty}^{+\infty}\delta(t-kT_s). \tag{A2}$$

According to Shannon's sampling theorem, we obtain

$$\begin{aligned}\hat{d}(s)&=\hat{d}(s+jn\omega_s)\\&=-F_m^-\sum_{n=-\infty}^{+\infty}\left(\hat{i}_s(s+jn\omega_s)e^{-(s+jn\omega_s)\varepsilon}\right)\end{aligned} \tag{A3}$$

$$\begin{aligned}\hat{d}(s)&=\hat{d}(s+jn\omega_s)\\&=-F_m^+\sum_{n=-\infty}^{+\infty}\left(\hat{i}_s(s+jn\omega_s)e^{(s+jn\omega_s)\varepsilon}\right).\end{aligned} \tag{A4}$$

Processing (A3) and (A4) in the same way as (6), we can get the expressions of $G_{\mathrm{PWM}}(s)$ as shown in (A5) and (A6) as follows:

$$G_{\mathrm{PWM\_a}}^-(s)=\frac{F_m^-}{1+F_m^-H_i\sum_{n=-\infty,n\neq0}^{+\infty}\left(G_{\mathrm{id\_a}}(s+jn\omega_s)e^{-(s+jn\omega_s)\varepsilon}\right)}$$

$$T_{c\_\mathrm{Li}}(s)=\frac{\hat{v}_{\mathrm{fb}}(s)}{\hat{v}_{\mathrm{ref}}(s)}=\frac{f_s\left(1-e^{-sT_s}\right)\left(1-e^{-sT_s}\right)\frac{V_{\mathrm{in}}}{L_f s}\frac{R_cC_f s+1}{C_f s}}{R_cm_1+\frac{m_c}{H_v}+\frac{m_1T_{\mathrm{on}}}{2C_f}+\left(-R_cm_1+R_cm_2-2\frac{m_c}{H_v}+\frac{m_1T_s+m_2T_{\mathrm{on}}}{C_f}\right)e^{-sT_s}+\left(-R_cm_2+\frac{m_c}{H_v}+\frac{m_2T_{\mathrm{off}}}{2C_f}\right)e^{-2sT_s}}$$
$$=\frac{\frac{V_{\mathrm{in}}}{L_{\mathrm{f}}s}\frac{R_cC_{\mathrm{f}}s+1}{C_{\mathrm{f}}s}f_sC_{\mathrm{f}}}{R_cC_{\mathrm{f}}m_1+\frac{m_1DT_{\mathrm{s}}}{2}+\frac{m_cC_{\mathrm{f}}}{H_{\mathrm{v}}}+(m_1+m_2)\left(\frac{T_{\mathrm{s}}}{e^{sT_{\mathrm{s}}}\left(1-e^{-sT_{\mathrm{s}}}\right)^2}+\frac{R_cC_{\mathrm{f}}}{e^{sT_{\mathrm{s}}}-1}\right)}=\frac{G_{\mathrm{vd\_a}}(s)}{\frac{1}{F_{\mathrm{m}}H_{\mathrm{v}}}+\frac{m_1+m_2}{C_{\mathrm{f}}}\left(\frac{R_cC_{\mathrm{f}}\pi}{j\omega_{\mathrm{s}}}\cot\left(\pi\frac{s}{j\omega_{\mathrm{s}}}\right)+\frac{1}{(j\omega_{\mathrm{s}})^2}\frac{\pi^2}{\sin^2(\pi s/j\omega_{\mathrm{s}})}\right)}} \tag{A14}$$

$$=\frac{F_m^-}{1+F_m^-(m_1+m_2)\left(\pi\cot(\pi s/j\omega_s)-\frac{1}{2}T_s-\frac{1}{s}\right)} \tag{A5}$$

$$G^+_{\mathrm{PWM\_}a}(s)=\frac{F_m^+}{1+F_m^+H_i\sum_{n=-\infty,n\neq0}^{+\infty}\left(G_{\mathrm{id\_}a}(s+jn\omega_s)e^{(s+jn\omega_s)\varepsilon}\right)}$$
$$=\frac{F_m^+}{1+F_m^+(m_1+m_2)\left(\pi\cot(\pi s/j\omega_s)+\frac{1}{2}T_s-\frac{1}{s}\right)} \tag{A6}$$

where the following infinite sum formulas are used in the derivation process. Note that $\varepsilon\neq0$ and $\varepsilon\to0^+$.

$$\begin{cases}\frac{1}{j\omega_s}\left(\sum_{n=-\infty}^{+\infty}\frac{e^{-(s+jn\omega_s)\varepsilon}}{s/j\omega_s+n}\right)-\frac{e^{-s\varepsilon}}{s}=\frac{\pi\cot(\pi s/j\omega_s)}{j\omega_s}-\frac{1}{2}T_s-\frac{1}{s}\\ \frac{1}{j\omega_s}\left(\sum_{n=-\infty}^{+\infty}\frac{e^{(s+jn\omega_s)\varepsilon}}{s/j\omega_s+n}\right)-\frac{e^{s\varepsilon}}{s}=\frac{\pi\cot(\pi s/j\omega_s)}{j\omega_s}+\frac{1}{2}T_s-\frac{1}{s}.\end{cases} \tag{A7}$$

Using the expression of F_m, F_m^-, and F_m^+

$$F_m=\frac{1}{\left(m_1-m_2/2+m_c\right)T_s},\ F_m^-=\frac{1}{(m_1+m_c)T_s},\ F_m^+=\frac{1}{(m_c-m_2)T_s}. \tag{A8}$$

We find that

$$\frac{F_m}{F_m^-}-F_m(m_1+m_2)\frac{1}{2}T_s=\frac{F_m}{F_m^+}+F_m(m_1+m_2)\frac{1}{2}T_s=1. \tag{A9}$$

According to (A9), (A5) and (A6) can be rearranged into the result given in (14), i.e.,

$$G^-_{\mathrm{PWM\_}a}(s)=G^+_{\mathrm{PWM\_}a}(s)=\frac{F_m}{1+F_m(m_1+m_2)\left(\pi\cot(\pi s/j\omega_s)-\frac{1}{s}\right)}. \tag{A10}$$

In fact, the above two modeling methods can also be extended to the VCM/PVM/VVM control, but it may bring additional computational complexity because of the introduction of the item ε.

In addition, the expression of $T_{i\_\mathrm{Brown}}(s)$ given in [35] is repeated as

$$T_{i\_\mathrm{Brown}}(s)=H_iG_{\mathrm{id}}(s)\frac{F_m^-}{1+F_m^-(m_1+m_2)\left(\frac{T_s}{e^{sT_s}-1}-\frac{1}{s}\right)}. \tag{A11}$$

Using the following equality:

$$\frac{T_s}{e^{sT_s}-1}=\frac{T_s}{2}\left(\frac{2e^{-s\frac{1}{2}T_s}}{e^{s\frac{1}{2}T_s}-e^{-s\frac{1}{2}T_s}}\right)=\frac{T_s}{2}\left(\frac{e^{s\frac{1}{2}T_s}+e^{-s\frac{1}{2}T_s}}{e^{s\frac{1}{2}T_s}-e^{-s\frac{1}{2}T_s}}-1\right)$$
$$=\frac{\pi}{j\omega_s}\cot\left(\pi\frac{s}{j\omega_s}\right)-\frac{1}{2}T_s \tag{A12}$$

one can easily find that the $T_{i\_\mathrm{Brown}}(s)$ is the same as the result represented by (15).

APPENDIX II

This appendix proves the equivalence between the $T_{c\_\mathrm{Li}}(s)$ and the expression in (50). Using (31), (38), (A12), and the equality

$$\sin^2\left(\pi\frac{s}{j\omega_s}\right)=\left(\frac{e^{s\frac{1}{2}T_s}-e^{-s\frac{1}{2}T_s}}{j2}\right)^2=-\frac{1}{4}e^{sT_s}\left(1-e^{-sT_s}\right)^2. \tag{A13}$$

$T_{c\_\mathrm{Li}}(s)$ for the PVM controlled buck converter with $H_v\neq1$ (see [29, Table 4.2]) can be rearranged into the form given in (50) as shown in (A14), which can be found at the top of this page.

REFERENCES

[1] W. Huang, "A new control for multi-phase buck converter with fast transient response," in *Proc. 16th Annu. IEEE Appl. Power Electron. Conf. Expo.*, 2001, pp. 273–279.

[2] "Adaptive constant on-time (D-CAP$^{\mathrm{TM}}$) control study in notebook applications," TI document, Jul. 2007. [Online]. Available: https://www.ti.com/lit/an/slva281b/slva281b.pdf

[3] "Control-mode quick reference guide," TI document, 2017. [Online]. Available: https://www.ti.com/lit/sg/slyt710a/slyt710a.pdf

[4] W. Huang, L. Liu, X. Liao, C. Xu, and Y. Li, "A 240-nA quiescent current, 95.8% efficiency AOT-controlled buck converter with A2-comparator and sleep-time detector for IoT application," *IEEE Trans. Power Electron.*, vol. 36, no. 11, pp. 12898–12909, Nov. 2021.

[5] J. Sun, "Characterization and performance comparison of ripple-based control for voltage regulator modules," *IEEE Trans. Power Electron.*, vol. 21, no. 2, pp. 346–353, Mar. 2006.

[6] R. Redl and J. Sun, "Ripple-based control of switching regulators—An overview," *IEEE Trans. Power Electron.*, vol. 24, no. 12, pp. 2669–2680, Dec. 2009.

[7] B. Cheng, E. Lee, B. Lynch, and T. Robert, "Choosing the right variable frequency buck regulator control strategy," TI Power Supply Design Seminar, 2014. [Online]. Available: https://www.ti.com/seclit/wp/slup319/slup319.pdf

[8] G. W. Wester, "Low-frequency characterization of switched dc-dc converter," Ph.D. dissertation, Dept. Elect. Eng., Caltech, Pasadena, CA, USA, 1972.

[9] J. Sun and R. M. Bass, "Modeling and practical design issues for average current control," in *Proc. 14th Annu. IEEE Appl. Power Electron. Conf. Expo.*, 1999, pp. 980–986.

[10] S. M. Cuk, "Modeling, analysis, and design of switching converters," Ph.D. dissertation, Dept. Elect. Eng., Caltech, Pasadena, CA, USA, 1976.

[11] R. W. Erickson and D. Maksimovic, *Fundamentals of Power Electronics*, 2nd ed. Norwell, MA, USA: Kluwer Academic Publishers, 2001.

[12] C. W. Deisch, "Simple switching control method changes power converter into a current source," in *Proc. IEEE Power Electron. Specialists Conf.*, 1978, pp. 300–306.

[13] R. Redl, "Small-signal high-frequency analysis of the free-running current-mode-controlled converter," in *Proc. 22nd Annu. IEEE Power Electron. Specialists Conf.*, 1991, pp. 897–906.
[14] D. Goder, "Switching regulator," U.S. Patent 5 770 940, Jun. 23, 1998.
[15] J. Sun, "Small-signal modeling of variable-frequency pulsewidth modulators," *IEEE Trans. Aerosp. Electron. Syst.*, vol. 38, no. 3, pp. 1104–1108, Jul. 2002.
[16] C. Fang and R. Redl, "Subharmonic stability limits for the buck converter with ripple-based constant on-time control and feedback filter," *IEEE Trans. Power Electron.*, vol. 29, no. 4, pp. 2135–2142, Apr. 2014.
[17] J. Sun and R. M. Bass, "A new approach to averaged modeling of PWM converters with current-mode control," in *Proc. 23rd IEEE Int. Conf. Ind. Electron. Control Instrum.*, 1997, pp. 599–604.
[18] R. B. Ridley, "A new small-signal model for current-mode control," Ph.D. dissertation, Dept. Elect. Eng., Virginia Tech, Blacksburg, VA, USA, 1990.
[19] F. D. Tan, "Modeling and control of switching converters: I. Unified modeling and measurement of current-programmed converters," Ph.D. dissertation, Dept. Elect. Eng., Caltech, Pasadena, CA, USA, 1993.
[20] D. J. Perreault and G. C. Verghese, "Time-varying effects and averaging issues in models for current-mode control," *IEEE Trans. Power Electron.*, vol. 12, no. 3, pp. 453–461, May 1997.
[21] B. Bryant and M. K. Kazimierczuk, "Sample and hold effect in PWM DC-DC converters with peak current-mode control," in *Proc. IEEE Int. Symp. Circuits Syst.*, 2004, pp. V–860–V–863.
[22] C. Fang and R. Redl, "Subharmonic instability limits for the peak-current-controlled buck converter with closed voltage feedback loop," *IEEE Trans. Power Electron.*, vol. 30, no. 2, pp. 1085–1092, Feb. 2015.
[23] A. R. Brown and R. D. Middlebrook, "Sampled-data modeling of switching regulators," in *Proc. IEEE Power Electron. Specialists Conf.*, 1981, pp. 349–369.
[24] R. B. Ridley, "A new, continuous-time model for current-mode control," *IEEE Trans. Power Electron.*, vol. 6, no. 2, pp. 271–280, Apr. 1991.
[25] S. Hsu, A. R. Brown, L. Rensink, and R. D. Middlebrook, "Modelling and analysis of switching dc-to-dc converters in constant-frequency current-programmed mode," in *Proc. IEEE Power Electron. Specialists Conf.*, 1979, pp. 284–301.
[26] J. Sun and C. Byungcho, "Averaged modeling and switching instability prediction for peak current control," in *Proc. IEEE 36th Power Electron. Specialists Conf.*, 2005, pp. 2764–2770.
[27] G. C. Verghese, C. A. Bruzos, and K. N. Mahabir, "Averaged and sampled-data models for current mode control: A re-examination," in *Proc. 20th Annu. IEEE Power Electron. Specialists Conf.*, 1989, pp. 484–491.
[28] F. D. Tan and R. D. Middlebrook, "A unified model for current- programmed converters," *IEEE Trans. Power Electron.*, vol. 10, no. 4, pp. 397–408, Jul. 1995.
[29] J. Li, "Current-mode control: Modeling and its digital application," Ph.D. dissertation, Dept. Elect. Eng., Virginia Tech, Blacksburg, VA, USA, 2009.
[30] S. Qu, "Modeling and design considerations of V^2 controlled buck regulator," in *Proc. 16th Annu. IEEE Appl. Power Electron. Conf. Expo.*, 2001, pp. 507–513.
[31] M. Leng, G. Zhou, Q. Tian, G. Xu, and X. Zhang, "Improved small-signal model for switching converter with ripple-based control," *IEEE Trans Ind. Electron.,* vol. 68, no. 1, pp. 222–235, Jan. 2021.
[32] S. Tian, "Equivalent circuit model of high frequency pulse-width- modulation (PWM) and resonant converters," Ph.D. dissertation, Dept. Elect. Eng., Virginia Tech, Blacksburg, VA, USA, 2015.
[33] Y. Yan, "Equivalent circuit model for current mode controls and its extensions," Ph.D. dissertation, Dept. Elect. Eng., Virginia Tech, Blacksburg, VA, USA, 2013.
[34] P. Liu, "Advanced control schemes for high-bandwidth multiphase voltage regulators," Ph.D. dissertation, Dept. Elect. Eng., Virginia Tech, Blacksburg, VA, USA, 2015.
[35] A. R. Brown, "Topics in the analysis, measurement, and design of high-performance switching regulators," Ph.D. dissertation, Dept. Elect. Eng., Caltech, Pasadena, CA, USA, 1981.
[36] Y. Qiu, M. Xu, K. Yao, J. Sun, and F. C. Lee, "Multifrequency small-signal model for buck and multiphase buck converters," *IEEE Trans. Power Electron.*, vol. 21, no. 5, pp. 1185–1192, Sep. 2006.
[37] X. Li, X. Ruan, Q. Jin, M. Sha, and C. K. Tse, "Small-signal models with extended frequency range for dc–dc converters with large modulation ripple amplitude," *IEEE Trans. Power Electron.*, vol. 33, no. 9, pp. 8151–8163, Sep. 2018.
[38] S. Hsiao, D. Chen, C. Chen, and H. Nien, "A new multiple-frequency small-signal model for high-bandwidth computer V-core regulator applications," *IEEE Trans. Power Electron.*, vol. 31, no. 1, pp. 733–742, Jan. 2016.
[39] C. L. Phillips, J. M. Parr, and E. A. Riskin, *Signals, Systems, and Transforms*, 4th ed. Upper Saddle River, NJ, USA: Pearson Education, 2008.
[40] R. D. Middlebrook and S. Cuk, "A general unified approach to modelling switching-converter power stages," in *Proc. IEEE Power Electron. Specialists Conf.*, 1976, pp. 18–34.
[41] G. W. Wester and R. D. Middlebrook, "Low-frequency characterization of switched dc-dc converters," *IEEE Trans. Aerosp. Electron. Syst.*, vol. AES-9, no. 3, pp. 376–385, May 1973.
[42] L. B. W. Jolley, *Summation of Series*, 2nd ed. Toronto, ON, Canada: Dover, 2014, pp. 144–152.
[43] 2014. [Online]. Available: https://math.stackexchange.com/questions/637169/taylor-series-for-cot-x
[44] 2016. [Online]. Available: https://math.stackexchange.com/questions/1940797/taylor-series-of-frac1-sinz-and-frac1-tanz
[45] R. Tymerski, "Frequency analysis of time-interval-modulated switched networks," *IEEE Trans. Power Electron.*, vol. 6, no. 2, pp. 287–295, Apr. 1991.
[46] R. Tymerski, "Application of the time-varying transfer function for exact small-signal analysis," *IEEE Trans. Power Electron.*, vol. 9, no. 2, pp. 196–205, Mar. 1994.

Na Yan received the B.S. degree in electrical engineering from Northeastern University, Shenyang, China, in 2014. She is currently working toward the Ph.D. degree in electrical engineering with the Nanjing University of Aeronautics and Astronautics, Nanjing, China.

Her research interests include point-of-load power converters, dynamic modeling, and control of power electronics.

Xinbo Ruan (Fellow, IEEE) received the B.S. and Ph.D. degrees in electrical engineering from the Nanjing University of Aeronautics and Astronautics (NUAA), Nanjing, China, in 1991 and 1996, respectively.

In 1996, he was with the Faculty of Electrical Engineering Teaching and Research Division, NUAA, where he became a Professor with the College of Automation Engineering, in 2002, and has been engaged in teaching and research in the field of power electronics. From August 2007 to October 2007, he was a Research Fellow with the Department of Electronic and Information Engineering, Hong Kong Polytechnic University, Hong Kong. From March 2008 to September 2011, he was also with the School of Electrical and Electronic Engineering, Huazhong University of Science and Technology, Wuhan, China. He has authored or coauthored 11 books and more than 300 technical papers published in journals and conferences. His research interests include soft-switching dc–dc converters, soft-switching inverters, power factor correction converters, modeling the converters, power electronics system integration, and renewable energy generation system.

Prof. Ruan was a recipient of the Delta Scholarship by the Delta Environment and Education Fund in 2003 and was a recipient of the Special Appointed Professor of the Chang Jiang Scholars Program by the Ministry of Education, China, in 2007. From 2005 to 2013, and since 2017 again, he has been a Vice President of the China Power Supply Society. Since 2008, he has been a member of the Technical Committee on Renewable Energy Systems within the IEEE Industrial Electronics Society. He is currently an Associate Editor for the IEEE TRANSACTIONS ON INDUSTRIAL ELECTRONICS, IEEE TRANSACTIONS ON POWER ELECTRONICS, *IEEE Journal of Emerging and Selected Topics on Power Electronics*, the IEEE TRANSACTIONS ON CIRCUITS AND SYSTEMS—II, and the *Open Journal of the IEEE Industrial Electronics Society*.

Xin Li (Member, IEEE) received the B.S. and Ph.D. degrees in electrical engineering and automation from the Nanjing University of Aeronautics and Astronautics, Nanjing, China, in 2012 and 2018, respectively.

In 2019, he worked as a Research Engineer with Huawei Technologies Co., Ltd., Shanghai, China. Since 2020, he has been a Research Fellow with Nanyang Technological University, Singapore. His research interests include modeling, control and design of PWM converter, resonant converter, and wireless power transfer system.